Design and Analysis of Optomechanical Micro Gyroscope for Angular-Vibration Detection

Jamal N. A. Hassan *, Wenyi Huang , Xing Yan , Senyu Zhang , Dingwei Chen , Guangjun Wen , Yongjun Huang *

Posted Date: 8 October 2023

doi: 10.20944/preprints202310.0445.v1

Keywords: Micro-gyroscopes; optomechanical; photonic crystal; angular vibration; dual-frame

Article

Design and Analysis of Optomechanical Micro Gyroscope for Angular-Vibration Detection

Jamal N. A. Hassan *, Wenyi Huang, Xing Yan, Senyu Zhang, Dingwei Chen, Guangjun Wen and Yongjun Huang *

School of Information and Communication Engineering, Sichuan Provincial Engineering Research Center of Communication Technology for Intelligent IoT, University of Electronic Science and Technology of China, Chengdu, 611731, China

* Correspondence: Yongjun Huang, E-mail: yongjunh@uestc.edu.cn, Jamal N. A. Hassan, E-mail: jamal1almelhany@gmail.com

Abstract: Micro-gyroscopes based on the Coriolis principle are widely employed in inertial navigation, motion control, and vibration analysis applications. This paper presents our main contributions which include a novel dual-frame optomechanical gyroscope, a unique photonic crystal cavity design, and advanced numerical simulation and optimization methods. The proposed design utilizes an optical cavity formed between dual oscillating frames, whereby input rotation induces a measurable phase shift via optomechanical coupling. Actuation of the frames is achieved electrostatically via an interdigitated comb-drive design. Through theoretical modeling based on cavity optomechanics and finite element simulation, the operating principle and performance parameters are evaluated in detail. Results indicate an expected angular rate sensitivity of 22.8 mV/°/s and angle random walk of 7.1×10^{-5} °/$h^{1/2}$, representing superior precision than to existing micro-electromechanical systems gyroscopes of comparable scale. Detailed analysis of the optomechanical transduction mechanism suggests this dual-frame approach could enable angular vibration detection with resolution exceeding state-of-the-art solutions.

Keywords: Micro-gyroscopes; optomechanical; photonic crystal; angular vibration; dual-frame

1. Introduction

Gyroscope, as a kind of inertial sensor that can measure the angular velocity and angular vibration, has wide-ranging applications in aerospace, industrial automation, and structural health monitoring where rotational or angular motion must be precisely tracked [1–3]. Over recent decades, micro-electromechanical systems (MEMS) gyroscopes leveraging the Coriolis effect have become particularly prevalent due to the ability to miniaturize sensitive elements using microfabrication techniques. Based on structural configuration, MEMS gyroscopes typically fall into one of several categories, including framed resonators, vibrating beams or loops, and ring resonators [4–7]. Within framed designs, single, double, and multi-mass block implementations have been developed to modulate Coriolis forces [8–11]. Narrow down to the specific problem or gap that the study aims to address, such as the limitations of traditional MEMS gyroscopes that rely on electronic transduction and noise sources. Effects such as thermal fluctuations, material stresses, and electromagnetic interference (EMI) introduce uncertainties that constrain achievable measurement sensitivity and accuracy levels [12].

While MEMS sensors effectively enable linear vibration monitoring, conventional MEMS gyroscopes have seen limited application in angular vibration measurement due to typical resolutions on the order of microradians [13–16]. However, recent advances integrating micro-opto-electromechanical systems (MOEMS) have prompted new gyroscopic designs capable of pushing these boundaries. Specifically, optomechanical systems leveraging cavity-enhanced transduction have emerged as a versatile tool for sensing myriad physical quantities including displacement, mass, acceleration, and gravitational waves at micro/nano scales [17–22]. Notably, the Coriolis effect intrinsic to gyroscopic sensing allows input angular vibrations to modulate an optomechanical cavity,

 doi:10.20944/preprints202310.0445.v1

translating rotations into detectable changes in optical properties. This characteristic provides a conceptual basis for establishing a novel class of high-precision gyroscopes optimized for angular vibration detection [23–25]. However, prior works in this domain have focused primarily on theoretical descriptions, leaving a need for concrete device architectures capable of experimentally validating the potential of this sensing modality. The current study aims to address this gap by proposing and numerically characterizing a dual-mass optomechanical gyroscope design, establishing a pathway toward next-generation inertial sensors affording resolutions surpassing state-of-the-art MEMS solutions.

In this paper, a novel dual-frame optomechanical gyroscope architecture utilizing a photonic crystal cavity is presented. Through rigorous theoretical analysis grounded in optomechanical coupling principles, the detailed operating mechanism and transduction processes of the proposed design are elucidated. Complimenting this, finite element modeling is employed to numerically characterize both the mechanical behavior of the sensing element as well as the optical properties emerging from the photonic crystal structure. By leveraging simulations, key figures of merit such as the scale factor relating output signals to input rotations and the fundamental noise floor limitations are computationally predicted. These performance metrics indicate the potential for this optomechanical gyroscope design to achieve angular resolutions sur-passing existing MEMS-based solutions when implemented in an experimental setting. More broadly, the presented analyses establish a conceptual and analytical framework for future efforts to optimize optomechanical inertial sensors targeting high-precision angular vibration measurement. With further refinement, this dual-frame approach may ultimately fulfill the long-sought goal of inertial sensors integrating microscale form factors with nanoradian-level angular sensitivity.

2. Operation Principle

2.1. Dual-frame optomechanical gyroscope architecture design

The proposed dual-frame optomechanical gyroscope design consists of three primary components as depicted in Figure 1a: an actuation element, sensing element, and detection module. The actuation element utilizes an electrostatic comb drive structure to induce resonance in the outer mass block via electrostatic pull-off forces. The sensing element is comprised of a central mass block suspended by straight and U-shaped flexural beams. The straight beams connect the outer block to the substrate while the U-shaped beams tether it to the central block. Critically, this central block acts as the inertial element whose Coriolis-induced deflections encode the input angular motion. For detection, a photonic crystal optomechanical cavity is integrated between the central and outer mass blocks. Variations in the cavity length modulated by the sensing element's resonant motion can be optically interrogated. Specifically, shifts in the cavity resonance wavelength provide a measurable proxy for angular motion. By segregating driving, sensing, and readout functions into distinct yet interfaced components, this dual-frame gyroscope design aims to leverage the advantages of optical transduction while maintaining essential characteristics such as narrowband actuation and wide dynamic range inertial sensing enabled by its mechanical architecture. The following sections will characterize these elements in further detail.

Preprints (www.preprints.org) | NOT PEER-REVIEWED | Posted: 8 October 2023 doi:10.20944/preprints202310.0445.v1

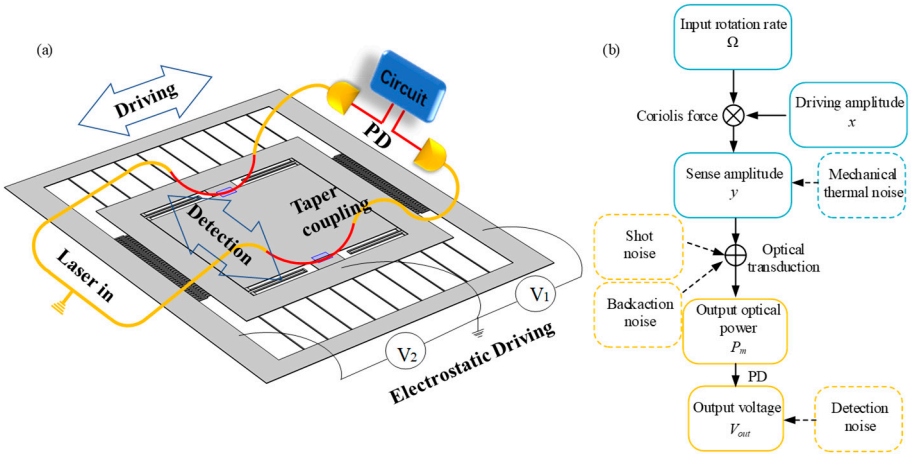

Figure 1. (a) The overall schematic diagram of the optomechanical micro-gyroscope, (b) block diagram of a signal processing sequence in an optical sensing system.

Second, in the angular rate detection configuration, an electrostatic driving force induces simultaneous resonant oscillation of the outer and central masses along the horizontal x-axis. Upon exposure to an external angular vibration about the z-axis, Coriolis forces perturb the central mass perpendicular to its driving mode, generating y-axis vibrations. Specifically, as the central mass oscillates at its resonant frequency f_x, any imposed rotation Ω_z yields a Coriolis acceleration of $-2(f_x\Omega_z)$ directed along the orthogonal y-axis. This modulation imprints the input angular frequency information onto the central mass's y-axis deflection profile. Crucially, as the central mass vibrates in both x and y, it modulates the interfaced optomechanical cavity in two orthogonal directions. By monitoring this cavity length perturbation at both f_x and f_y, the amplitude and phase relationship between the driving and Coriolis-induced responses can be resolved. This dual-axis transduction scheme thus enables separating angular rate signals from other sources of detection noise or spurious vibrations, establishing the basis for precision Coriolis-effect gyroscope.

Third, optical interrogation of the dual-mass gyroscope is facilitated using a photonic crystal optomechanical cavity integrated between the central and outer masses. Light from an external laser source is coupled into the cavity via an on-chip waveguide or fiber optic connection. Under the influence of Coriolis-induced vibrations, the central mass oscillates orthogonally to vary the effective cavity length. This modulation manifests as shifts in the cavity's transmission spectrum according to the principles of cavity optomechanics. Specifically, deviations in resonant wavelength $\Delta\lambda$ from the cavity's rest state are proportional to changes in gap width Δx induced by Coriolis oscillations of the central mass. Optical power transmitted by the cavity is thereby encoded with information about the input angular rate. A photodetector then converts the modulated optical transmission into an electrical voltage signal v(t) oscillating at the Coriolis frequency ω_y. As illustrated by the block diagram in Figure 1b, shows a block diagram of a signal processing sequence in the MOEMS sensor. Proper characterization of the optomechanical transduction thus enables angular velocity to be resolved from the photodetector voltage with suitable signal conditioning and processing.

2.2. Theoretical description of optomechanical coupling

Optomechanical cavities are commonly interfaced using tapered optical waveguides or fibers to facilitate light coupling and output, as shown in Figure 2a. The fundamental cavity-waveguide interaction dynamics are governed by input-output relations derived from classical cavity optomechanics theory [26,27]. Specifically, the intra-cavity optical field amplitude 'a' experiences external coupling to the waveguide/fiber at a rate κ_e, as well as intrinsic dissipation to the surrounding environment at a rate κ_i. These rates characterize the photon escape channels from the optical resonance and determine the cavity linewidth. Using the standard input-output framework [27], the steady-state response of the intra-cavity field 'a' to an input field amplitude 'a_{in}' is governed by:

Preprints (www.preprints.org) | NOT PEER-REVIEWED | Posted: 8 October 2023 doi:10.20944/preprints202310.0445.v1

$$\frac{da}{dt} = -i\Delta a - \frac{\kappa}{2}a + \sqrt{\kappa_e}a_{in} \quad (1)$$

where $\Delta = \omega_l - \omega_c$ represents the laser detuning rate of the laser resonant frequency ω_l and the optical cavity resonant frequency ω_c, $|a_{in}|^2 = P_{in}/\hbar\omega_l$, P_{in} is the input laser power, and $\hbar$ is the Planck constant. The total coupling rate κ is the sum of the external coupling rate and internal coupling rate, $\kappa = \kappa_e + \kappa_i$, and the optical quality factor is $Q_{opt} = \omega_c/\kappa$.

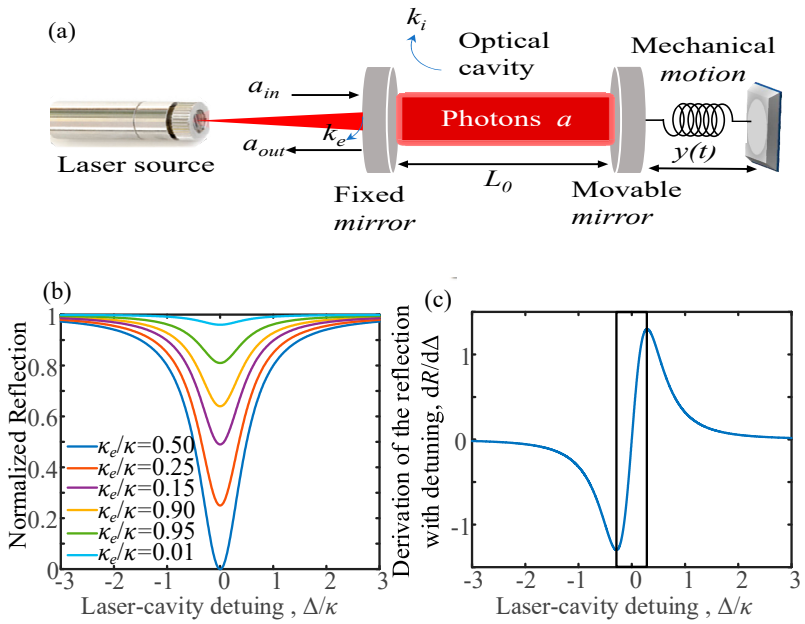

Figure 2. (a) Schematic diagram of a typical optomechanical system; (b) reflectance variation with detuning rate; (c) difference of reflectance variation with laser-cavity detuning rate.

This establishes the fundamental coupling between the waveguide/fiber and cavity modes which underpins optomechanical transduction in the gyroscope. Detailed characterization of κ_e, κ_i and their impact on cavity transmission/reflection will be critical for optimizing optical interface and readout schemes. The following sections aim to numerically simulate these cavity parameters and dynamics. Based on the steady-state condition (da /dt = 0), the intracavity field is:

$$a = \sqrt{\kappa_e}a_{in} \Big/ (i\Delta a + \frac{\kappa}{2}a) \quad (2)$$

Moreover, the output field is governed by the input and intracavity area [28],

$$a_{out} = -a_{in} + \sqrt{\kappa_e}a \quad (3)$$

Therefore, the normalized optical reflection R transmitted through waveguide is expressed as:

$$R = \left|a_{out}/a_{in}\right|^2 = 1 - \frac{k_e k_i}{\Delta^2 + k^2/4} \quad (4)$$

According to Eq. (4), the reflection spectrum presents a negative Lorentzian function in terms of laser-cavity detuning (seen in Figure 2b). We can see that the relationship between R and Δ can be divided into the under-coupling ($\kappa_e < \kappa/2$), critical-coupling ($\kappa_e = \kappa/2$), and over-coupling ($\kappa_e > \kappa/2$). Specifically, in under-coupling, R decreases from 1 to 0 with the increase of κ_e/κ from 0 to 1/2. With the rise of κ_e/κ from 1/2 to 1, the Lorentzian dip of R gradually disappears, and R returns to 1. In more exceptional cases, when κ_e/κ is much less than 1, almost no light is coupled into the optical cavity ($R \approx 1$). And when κ_e/κ is close to 1, all the light coupled into the optical cavity is almost not dissipated, and all the light coupling back to the waveguide ($R \approx 1$). However, in the critical coupling, all the light coupled into the optical cavity is dissipated in the environment, and the R is 0. Moreover, the amplitude variation relation of dR/dΔ is further studied, and the maximum value of dR/dΔ is directly shown in Figure 2c, which will be further discussed in Sec. II.C. It should be noted that due to the small and unstable R of the shaded area in Figure 2c (visually shown in Figure 2b), the locking cavity-laser detuning rate Δ should be kept away from the shaded area in practice. We reported the

Preprints (www.preprints.org) | NOT PEER-REVIEWED | Posted: 8 October 2023 doi:10.20944/preprints202310.0445.v1

uncertainty or error estimates for our simulation results by calculating the standard deviation and confidence interval for each performance metric, such as the scale factor, angle random walk, and optomechanical coupling rate.

2.3. Optomechanical sensing of displacement & angular vibration

The proposed dual-frame optomechanical gyroscope possesses an orthogonalized structural configuration as illustrated in Figure 3a. Under idealized operating conditions, the decoupled design behaves as two independent single degree-of-freedom spring-mass-damping systems along orthogonal x and y axes. When functioning as an angular rate sensor, the gyroscope drivers the outer mass resonantly along the drive axis (*x-direction*) while the Coriolis force perturbs the central mass along the orthogonal detection axis (*y-direction*), as previously described. If the resulting vibrational displacements are assumed small enough to satisfy the linearization approximation, yet the driving motion remains much larger than the Coriolis response, the gyroscope dynamics can be expressed as two linearly coupled simple harmonic oscillators [29]:

$$\begin{cases} \ddot{x} + 2\xi\omega_x\dot{x} + \omega_x^2 x = F_{drive}/m_x \\ \ddot{y} + 2\xi\omega_y\dot{y} + \omega_y^2 y = F_{Coriolis}/m_y \end{cases} \quad (5)$$

where x and y are the displacements in driving and sensing directions respectively; ξ parametrizes damping, ω_x and ω_y are the angular resonant frequencies, m_x and m_y are the equivalent mass of the driving mode and detection mode; and the drive/Coriolis forces are treated as perturbations. Numerical simulation of these governing equations of motion will enable characterization of key performance metrics in subsequent sections. The Coriolis force $F_{Coriolis} = -2m_y\Omega x$, the gyroscope dynamics equations can be better described by:

$$\begin{cases} m_x\ddot{x}+c_x\dot{x}+k_x x=F_{drive} \\ m_y\ddot{y}+c_y\dot{y}+k_y y=-2m_y\Omega\dot{x} \end{cases} \quad (6)$$

where k_x, c_x, k_y and c_y are the coupled oscillator equations of motion contain stiffness and damping coefficients corresponding to the orthogonal driving and detection vibration modes. From linear systems theory, these spring and damping parameters are related to the effective mass m and angular resonant frequencies ω_x and ω_y through: $k_x=\omega_x^2 m_x$, $c_x=2\xi\omega_x$, $k_y=\omega_y^2 m_y$, $c_y=2\xi\omega_y$. Here dot notation signifies a derivative concerning time, and the external angular vibration imposed on the gyroscope is mathematically modeled as a harmonic function of time $\Omega = |\Omega| sin(\omega_\Omega t)$, ω_Ω is the frequency of angular vibration. This establishes the analytical basis for characterizing the gyroscope dynamics using physical system parameters like resonance frequencies, damping, and time-varying input angular rate excitation. The numerical solution of the governing equations will enable performance evaluation under varying conditions.

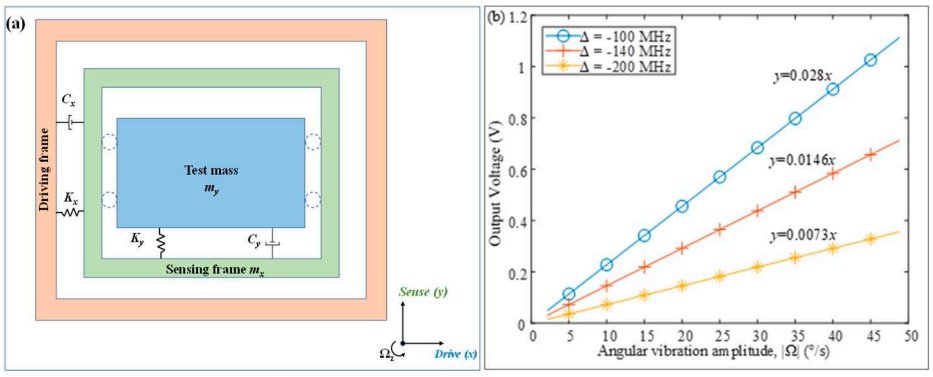

Figure 3. (a) Structure diagram of double decoupling gyroscope under ideal conditions; (b) output voltage of gyroscope variation with angular rate.

Preprints (www.preprints.org) | NOT PEER-REVIEWED | Posted: 8 October 2023 doi:10.20944/preprints202310.0445.v1

Based on Eq. (6), the displacement of the sensing mode is regarded as a harmonic motion under the stable condition:

$$y(t) = A\sin(\omega_\Omega t)\sin(\omega_0 t)$$
$$= \frac{1}{2}A\left(\cos((\omega_\Omega - \omega_0)t) - \cos((\omega_\Omega + \omega_0)t)\right) \quad (7)$$
$$A = \frac{-2|\Omega| F_{drive} Q_x}{m_x \omega_0 \sqrt{(\omega_y^2 - \omega_0^2) + \omega_y^2 \omega_0^2 / Q_y^2}}$$

where ω_0 is steady state frequency for driving mode, respectively, and Q_x, Q_y is the mechanical quality factors of the driving mode and sensing mode, respectively. Because the test range is limited, we just choose the low frequency of $y(t)$ to measure the amplitude and frequency of angular vibration, $y_{low}(t) = 0.5A\cos(\omega_\Omega - \omega_0)$.

As illustrated in (Figure 2a), the optical resonance frequency of the photonic crystal cavity is coupled to the mechanical vibrational motion of the dual-frame structure via the optomechanical interaction. In the linear response regime of small displacements, perturbation theory establishes that variations in cavity length $y(t)$ induce a shift in resonance frequency ω_c' that is linearly proportional to the displacement [28]. This relationship can be expressed as: $\omega_c' = \omega_c + g_{om}y(t)$, ω_c is the unperturbed cavity frequency at $y(t)=0$, and the optomechanical coupling rate $g_{om} = \partial\omega_c' / \partial y$ quantifies the transduction efficiency between mechanical and optical domains. By setting a fixed detuning between the laser drive frequency and ω_c, shifts in ω_c' due to vibrations along either orthogonal mechanical mode will manifest as changes in cavity transmission/reflection. A photodetector linked to the output waveguide can therefore resolve the amplitude and phase of both motional components by monitoring interference of the modulated optical signal. This dual-axis transduction scheme underlies the ability to isolate Coriolis-induced signals corresponding to input angular velocities, as discussed previously. Numerical simulation of these cavity dynamics will provide further insight into optomechanical performance.

The transmitted optical power P_m after interacting with the optomechanical system can be modeled based on the standard input-output relations of cavity optomechanics theory [30]. Specifically, for a laser driven at angular frequency ω_l that is coupled to an optical cavity of frequency ω_c with optomechanical coupling rate g_{om} and dissipation rates κ and γ_m, the steady-state mean cavity photon number $\langle n \rangle = (k/2)2/|(k/2)\text{-}i(\Delta\text{-}g_{om}y)|^2$ and output power P_m are given by:

$$P_m = P_{in}\eta\frac{dR}{dy}g_{om}y(t) = P_{in}\eta\frac{dR}{d\Delta}\frac{d\Delta}{dy}y(t) = P_{in}\eta\frac{dR}{d\Delta}g_{om}y(t) \quad (8)$$

where η represents some realistic losses from the cavity to the detector. Through the change of light power, the displacement of the gyroscope detection mode is detected, and the amplitude of angular vibration is calculated. The final total output voltage is shown in Figure 3b. The larger the angular vibration, the larger the voltage output, which is discussed in Sec. III.C. Numerically simulating equation (8) will allow characterization of how the output optical power P_m is modulated by the vibrational dynamics induced in the optomechanical cavity. This provides the theoretical framework for modeling optical transduction and readout in the gyroscope system.

3. Driving and sensing performance analysis

3.1. Design and analysis of driving and mechanical sensitive structure

Various actuation mechanisms have been implemented for resonantly driving the inertial masses in MEMS gyroscopes. Electrostatic comb drives represent a widely adopted solution due to advantages such as facile fabrication using standard microfabrication techniques, low power operation, and capacity for sufficient displacements. As illustrated in Figure 4a, a comb drive comprises interleaved fixed and movable sets of parallel electrodes (teeth). When an electrical potential is applied between the combs, electrostatic forces induce an oscillating transverse motion along the x-axis. The geometry is characterized by the overlap length l_f of opposing tooth surfaces, the width b_f of each tooth, and the gap distance a_f separating adjacent teeth.

Preprints (www.preprints.org) | NOT PEER-REVIEWED | Posted: 8 October 2023 doi:10.20944/preprints202310.0445.v1

The analytical model of comb drive actuation is well established [29]. Based on parallel plate capacitor theory, the resulting electrostatic force F_{drive} between a single tooth-pair is given by:

$$F_{drive} = \frac{4n\varepsilon_0 h U_d U_a \cos(\omega_d t)}{d} \quad (9)$$

where n is the number of comb teeth, h is the thickness, d is the parallel spacing between comb teeth, ε_0 is the vacuum dielectric constant. And U_d is the DC voltage set it as 5 V and the frequency of the driving force depends on the input AC electrical signal, $U_a \cos\omega_d t$ with U_a is 10 V.

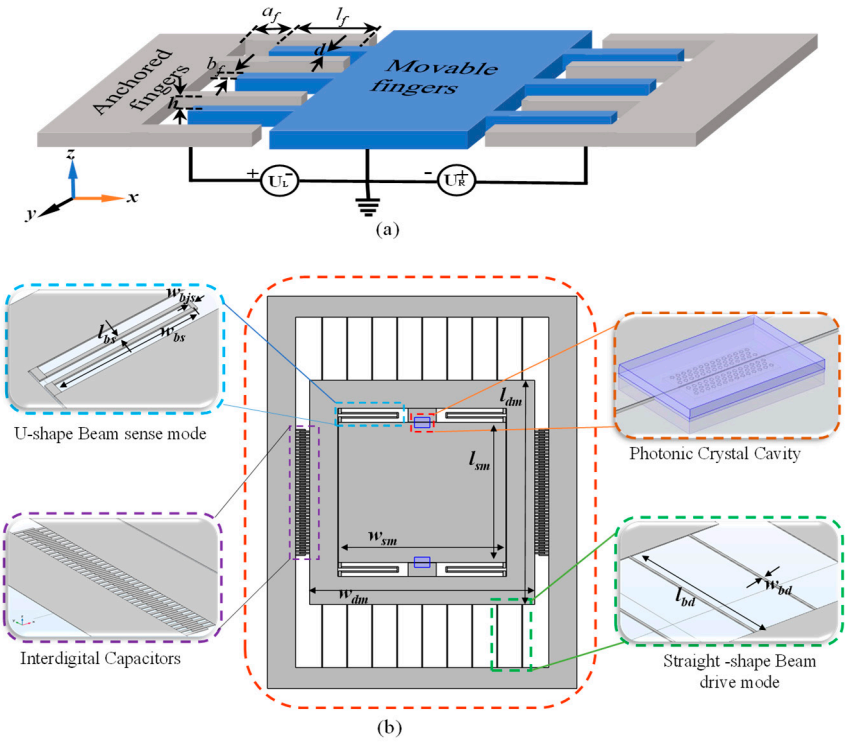

Figure 4. (a) Pull-off electrostatic comb driving structure diagram; (b) the structural design of the optomechanical micro-gyroscope.

A major consideration in the design of dual-mass optomechanical gyroscopes is decoupling the orthogonal driving and sensing vibrational modes to minimize cross-axis interference. The Coriolis force enables the rate output of a gyroscope by transferring drive motion into a detectable sense motion proportional to the input rate. According to design dimensions, the Coriolis force is 0.3855 rad/s.

This work presents a support structure employing U-shaped and folded flexure beams aimed at reducing equivalent stiffness and inter-modal coupling, as a shown in Figure 4b. Flexural beams are widely used in MEMS designs due to their ability to facilitate motion along defined axes while providing structural support. Prior work has shown that the stiffness of a U-shaped flexure beam K_{Ux} can be approximated as two straight beams connected in series for motion along the axis [29].

Specifically, the equivalent stiffness of the U-shaped beam in the driving x-direction is given by:

$$K_{Ux} = \left(\frac{EI}{l_1} + \frac{EI}{l_2}\right) - 1 = \mathrm{E}\frac{\mathrm{w}_{bd}^3 \mathrm{h}}{2\mathrm{l}_{bd}^3} \quad (10)$$

where K_x represents the stiffness coefficient; E is the Young's modulus, I is the cross-sectional moment of inertia, and l_1 and l_2 are the lengths of the individual straight segments respectively. w_{bd}, l_{bd} are width and length of the straight beam, respectively. It can be seen from Eq. (10) that the stiffness coefficient of a U-shaped beam is half that of a straight beam. Moreover, the structure can eliminate the residual stress generated by nano-machining and restrain the resonance frequency change brought by the residual stress. The analytical approach provides theoretical grounding for evaluating the proposed support architecture's effectiveness in decoupling modal responses.

Preprints (www.preprints.org) | NOT PEER-REVIEWED | Posted: 8 October 2023 doi:10.20944/preprints202310.0445.v1

Based on the analytical modeling presented, finite element analysis (FEA) was conducted to numerically simulate and optimize key design parameters of the gyroscope. Table 1 summarizes the optimized structural configuration obtained through this process. Generally, lower resonant frequencies benefit mechanical sensitivity but also susceptibility to external perturbations. Therefore, the driving and sensing modes were optimized to angular frequencies of 61969 Hz and 61811 Hz respectively for effective operation. Additionally, a thickness of *~250 nm* was chosen for the structural layers to realize the desired optical properties of the photonic crystal optomechanical cavity.

Table 1. Structural parameters of cavity optomechanical high precision micro gyroscope.

Symbol	Quantity	Value
$l_{Gyro} \times w_{Gyro}$	Gyro dimension	280 × 220 μm
h	Thickness of gyroscope	0.25 μm
l_{comb}	Comb-tooth capacitor length	1 μm
w_{comb}	Comb-tooth capacitor width	7 μm
l_{bd}	Driving beam length	45 μm
w_{bd}	Driving beam width	0.65 μm
l_{bs}	Sensing U-beam length	1 μm
w_{bs}	Sensing U-beam width	39.667 μm
l_{bjs}	Sensing U-beam join length	4 μm
w_{bjs}	Sensing U-beam join width	1 μm
d	Gap between comb teeth	500 nm
n	Number of comb teeth	40
l_{dm}	Drive mass length	160 μm
w_{dm}	Drive mass width	160 μm
w_{sm}	Sense mass width	119 μm
l_{sm}	Sense mass length	100 μm
Q	Mechanical Q-factor	10000

Gravitational effects can also impact device performance if mass blocks deform in response. As shown in Figure 5a,b, is necessary to simulate the maximum height difference caused by gravity. Through parameter studies, the maximum relative displacement between external and sensing masses under gravity load was constrained to less than *3.5 nm* at real length of inner beam. At this level, deflection poses negligible perturbation to either optical characteristics or optomechanical transduction.

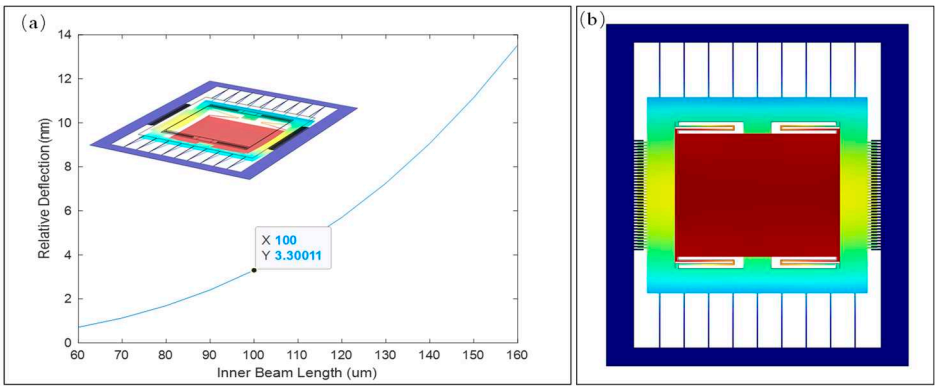

Figure 5. (a) calculating and simulating the gravitational deflection of the dual masses in an optomechanical gyroscope, (b) the simulation of z- axis displacement under gravity.

Based on the finite element analysis, the simulated gyroscope design allows further evaluation of driving performance and detection capabilities. Figure 6a demonstrates that increasing the number of comb electrodes and applied voltage augments the electrostatic driving force and resulting

Preprints (www.preprints.org) | NOT PEER-REVIEWED | Posted: 8 October 2023 doi:10.20944/preprints202310.0445.v1

displacements, as expected based on parallel plate capacitor theory. Figure 6b plots driving displacement versus excitation frequency, showing resonant behavior near 61969 Hz as per the optimized driving mode parameters. Peak displacement approaches 16 μm, sufficient for the intended operation. Equation (5) governs how Coriolis acceleration induced by external angular velocity is transduced to a sensed displacement. As seen in Figure 6c, this transduction efficiency decreases with a widening frequency split between driving and sensing resonances. However, packaging the device under vacuum conditions is expected to raise intrinsic Q factors, mitigating impacts from non-zero split. Overall, the simulated design metrics indicate the gyroscope concept could realize angular velocity detection within target specifications once fabricated and experimentally validated. Continued modeling will provide additional design insight.

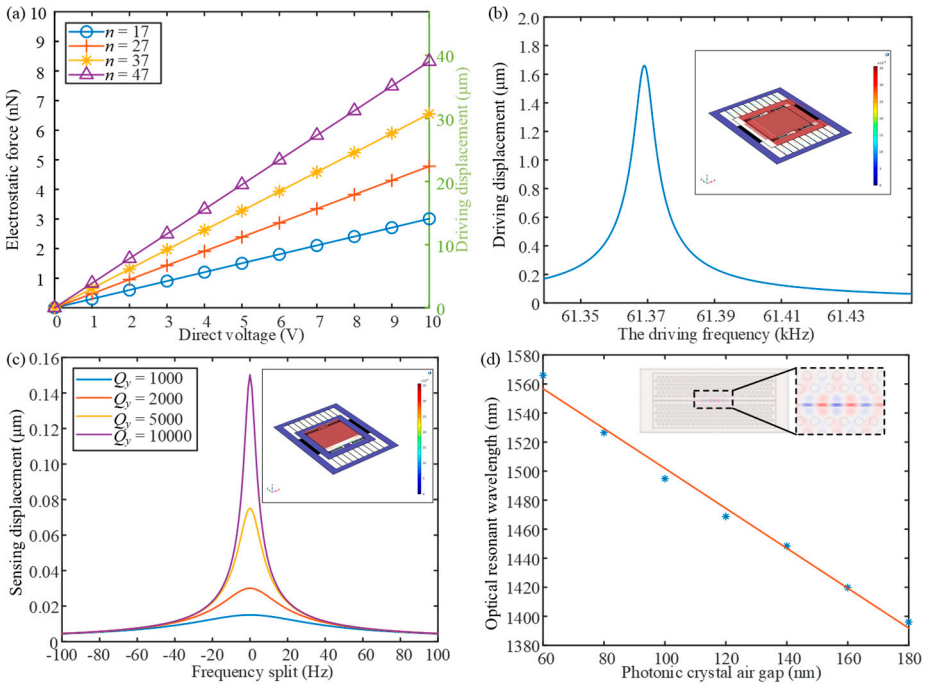

Figure 6. (a) The driving force and drive displacement change with the DC voltage; (b) The drive displacement varies with the drive frequency; (c) The sense displacement varies with the frequency split; (d) diagram of optical resonance wavelength variation with the width of photonic crystal air gap.

3.2. Simulation of photonic crystal cavity characteristics of optomechanical gyroscope

Based on the photonic crystal theory [31], we simulate the typical photonic crystal cavity performances by COMSOL and FDTD. The optical resonance frequency of the fundamental optical mode concerned in this paper is 200.69 THz, and the optical quality factor is 2.6e5.

Table 2. Structural parameters of photonic crystal.

Quantity	Value
Length of crystal	7 μm
Width of crystal	3.3 μm
Period of topology	470 nm
Air gap	100 nm
Distance between hole and air gap	438 nm
Distance between hole and center of structure	235 nm
Thickness of crystal	250 nm
Radius of hole	134 nm
Displacement of hole	5/10/15 nm

Preprints (www.preprints.org) | NOT PEER-REVIEWED | Posted: 8 October 2023 doi:10.20944/preprints202310.0445.v1

When the gyroscope is on working, the applied angular vibration will cause the gap width of the photonic crystal cavity to be changed. Therefore, it was found that the change in gap widths of the photonic crystal cavity would lead to a dispersion effect (optical system of the optomechanical micro-gyroscope, and signal processing sequence in an optical sensing system shown in the illustration in Figure 1). The simulated photonic crystal resonance wavelength with different gap widths is shown in Figure 6d.

3.3. Performance analysis of micro-gyroscope based on optomechanical system

The primary performances discussed in the paper for the micro gyroscope are scale factor (sensitivity) and angular random walk (noise limit). In general, a large-scale factor helps to improve the signal-to-noise ratio (SNR) and bias stability and increases the Coriolis coupling from the driving mode to the sensing mode. Besides, the noise limit consists of four parts: mechanical thermal noise [32], detection noise, shot noise, and back-action noise [30]. In the paper, the scale factor of the optomechanical gyroscope is the linear correlation between the output voltage V_{out} and the amplitude of the angular vibration $|\Omega|$. The total scale factor SF is composed of the mechanical sensitivity (S_m), the optomechanical sensitivity (S_P) of the cavity optomechanical system, and the voltage sensitivity (S_V) of the photodetector, which is expressed as:

$$SF = \frac{V_{out}}{|\Omega|} = S_{mech} \cdot S_P \cdot S_V \tag{11}$$

Based the Eq. (6), S_m is defined as the ratio of the displacement amplitude of the sensing mode to $|\Omega|$.

$$S_m = \left|\frac{0.5A}{\Omega}\right| = \frac{F_{drive} Q_x}{m_x \omega_0 \sqrt{(\omega_y^2 - \omega_0^2) + \omega_y^2 \omega_0^2 / Q_y^2}} \tag{12}$$

We have detailed the relationship between output power P_m and displacement of sensing mode in Sec. II.3. Therefore, based on Eq. (7), SP is expressed as:

$$S_p = \frac{P_m}{y} = P_{in} \frac{dR}{dy} \eta = P_{in} \eta \frac{dR}{d\Delta} g_{om} \tag{13}$$

In this paper, the PIN-TIA photodetector is selected, where S_V = 65 V/W. Besides, the random white noise in the system results in a zero-mean angel error, which is described by ARW. The ARW_{total} can characterize the short-term performance of the optomechanical gyroscope, which is:

$$ARW_{total} = \sqrt{ARW_{mech}^2 + ARW_{NEP}^2 + ARW_{SN}^2 + ARW_{ba}^2} \tag{14}$$

By substituting the equivalent thermal noise power spectral density of the proven mass into the mechanical motion equation (5), the ARW_{mech} is:

$$ARW_{mech} = \sqrt{\frac{4 k_B T e \omega_m Q_y}{m_y (Q_y^2 (-2\omega_m \omega_\Omega + \omega_\Omega^2)^2 + (\omega_m^2 - \omega_\Omega \omega_m)^2)}} \cdot \frac{1}{S_m} \tag{15}$$

where k_B is the Boltzmann constant, and Te is the temperature. The electronic noise of photodetectors is usually measured by noise equivalent optical power (NEP). Therefore, the equivalent ARW_{NEP} of an optomechanical gyroscope can be obtained by converting the equivalent noise at the output of the detector through scaling factors:

$$ARW_{NEP} = \frac{NEP}{P_{in} \eta \left|\frac{dR}{d\Delta} g_{om}\right| \cdot S_m} \tag{16}$$

Meanwhile, there also is shot noise in the laser light field obeying Poisson statistics, which can be converted to equivalent ARW:

$$ARW_{SN} = \frac{\sqrt{2\hbar \omega_\ell P_{\det} \eta_{qe}}}{P_{in} \eta \left|\frac{dR}{d\Delta} g_{om}\right| \cdot S_m} \tag{17}$$

Preprints (www.preprints.org) | NOT PEER-REVIEWED | Posted: 8 October 2023 doi:10.20944/preprints202310.0445.v1

where P_{det} and η_{qe} are the optical power and quantum efficiency of the detector, respectively. Besides, in the optomechanical system, the shot noise exerts the reaction force and causes the photonic crystal to move, which is the back-action noise:

$$ARW_{ba} = \frac{2\hbar g_{om} Q_y}{m_y S_m} \sqrt{\frac{2n_c}{\kappa(Q_y^2(-2\omega_m\omega_\Omega + \omega_\Omega^2)^2 + (\omega_m^2 - \omega_\Omega\omega_m)^2)}} \tag{18}$$

Based on the above theoretical analysis, the influence of input power and laser-cavity detuning on the gyroscope proposed in this paper is discussed in detail. Specifically, those parameters $\Delta = -\kappa/2$, $\kappa_e = 1.5\times10^8$, $\kappa_i = 0.5\times10^8$ and $g = 3$ GHz/nm are chosen in this paper for a joint optomechanical cavity. Because the optomechanical sensitivity changes linearly with the input laser power, the total sensitivity increases with the increase of the light power, and at the same time, the noise caused by the detector and shot noise decreases with the rise of the power (as seen in Figure 7a,b). Meanwhile, the number of photons in the cavity increases rapidly, resulting in the increased optomechanical coupling and a rise in the back-action noise. However, the shot noise, detection noise and back-action noise usually are smaller than mechanical thermal noise. Besides, the sensitivity can be significantly improved by choosing appropriate laser-cavity detuning, as shown in Figure 7c. When $\Delta = -\kappa/2$, the scale factor is 22.8 $mV/(°/s)$. As shown in Figure 7d, although all other noises except thermal noise are affected by laser-cavity detuning, ARW_{total} is mainly affected by mechanical thermal noise. Moreover, the mechanical thermal noise is Lorentzian function as the frequency. When the detection frequency deviates from the mechanical resonance frequency, the thermal noise will decrease rapidly due to the angular vibration frequency (as seen in Figure 8). However, the low-frequency noise of detector is considerable, which limits the bandwidth of angular vibration.

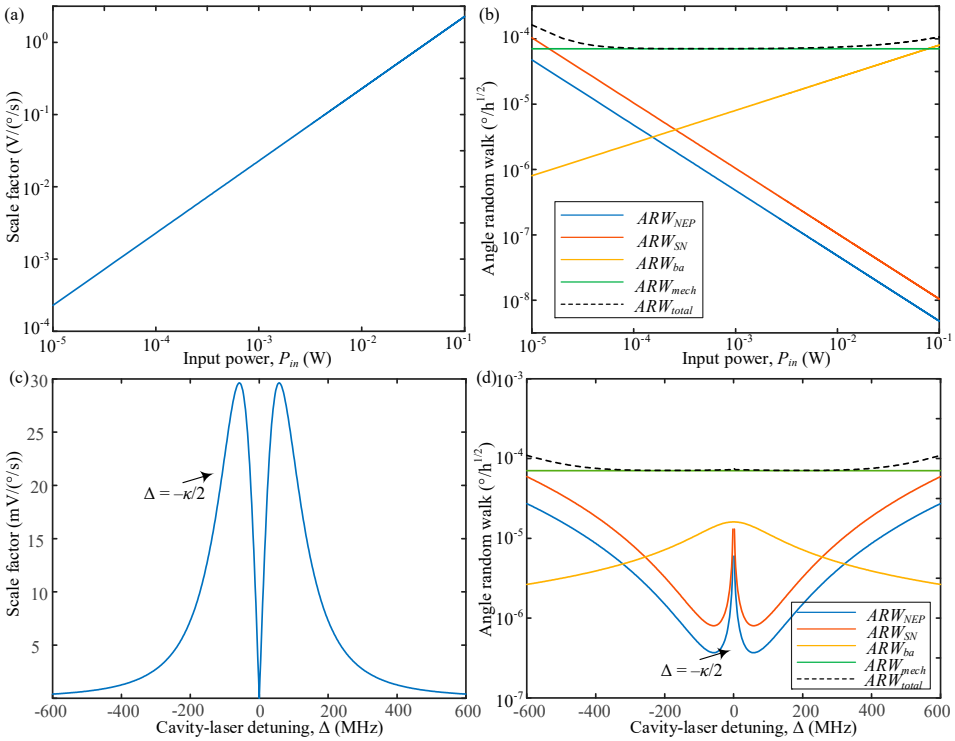

Figure 7. (a) Sensitivity and (b) angle random walk variation with the input laser power; (c) Sensitivity and (d) angle random walk variation with the detuning rate.

Preprints (www.preprints.org) | NOT PEER-REVIEWED | Posted: 8 October 2023 doi:10.20944/preprints202310.0445.v1

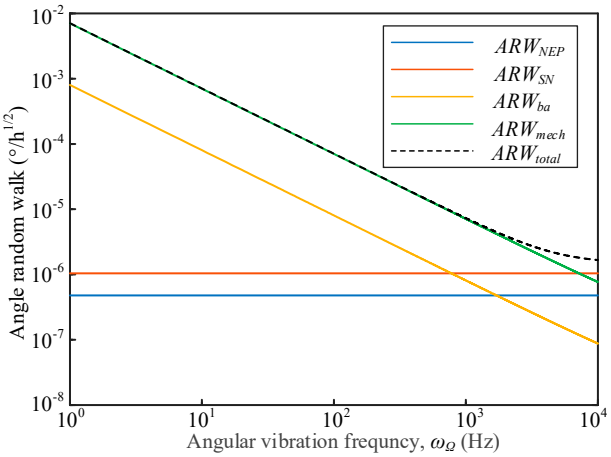

Figure 8. Angle random walk variation with the angular vibration frequency.

4. Comparative study

Several MEMS gyroscope designs have been proposed to achieve low noise and high-resolution rotational motion sensing. Recently they introduced a new family of ultra-high-Q silicon MEMS tuning fork gyroscopes that enabled interchangeable measurement of rotation rate and integrated angle [33]. This built upon prior works such as in [34] that achieved resolution of 7.1 ◦/s/Hz$^{1/2}$ using a triple-mass Z-axis design, but addressed thermal noise limitations of purely mechanical gyroscopes. presented dual and quadruple mass gyroscope architectures fabricated using SOI wafers, with the symmetric quadruple mass structure demonstrating virtually identical high Q factors of *0.86* million for the drive and sense modes. This balanced design allowed direct measurement of rotation angle without the bandwidth and dynamic range constraints of regular rate gyroscopes. Later, in [35] incorporated similar mass distribution concepts into their center-supported quadruple mass gyroscope to minimize errors. However, these works by previous studies mentioned above. still relied on capacitive or piezoresistive sensing schemes that introduced electronic noise. More recently, they presented a novel MOEMS gyroscope integrating optical detection on a hybrid MEMS-photonic platform to reduce such thermal fluctuations through cavity optomechanics [36]. The optomechanical gyroscope based on the optical cavity designed in this paper can achieve ultra-high Q-factors exceeding 10^{10}, orders of magnitude better than the reported MEMS designs. All-optical operation is well-suited for miniaturization and integration on photonic chips for robust, low power inertial sensing in consumer, automotive and aerospace applications.

Preprints (www.preprints.org) | NOT PEER-REVIEWED | Posted: 8 October 2023 doi:10.20944/preprints202310.0445.v1

Gyroscope type	Structure	Proof mass	Resonator size	Driving method	Sensitivity	ARW (°/h1/2)
Quadruple mass MEMS gyroscope [33]	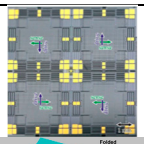	24.3 ng	2.7×2.7 mm	Electrostatic comb electrodes	1 nm /(◦/h)	-
A triple mass decoupled Z-axis micro-machined gyroscope [34]	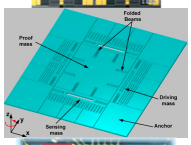	0.21 mg	4.6 × 4.6 mm	Electrostatic comb electrodes	17.5 μV/√Hz	-
CSQMG [35]	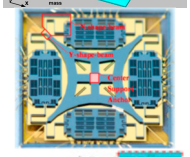	0.58 mg	7700 x 7700 μm	Electrostatic comb electrodes	20,209.2 LSB/(◦/s)	-
MOEMS [36]	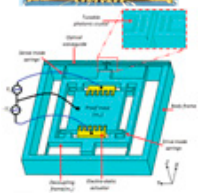	15μg	405 μm2	Electrostatic comb electrodes	0.051 nm/(◦ /s)	-
OMEMS	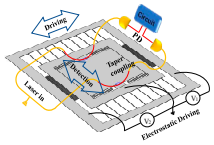	14 ng	280 × 220 μm	Optomechanical and comb electrodes for driving	22.8 mV/(◦/s)	7.1×10^{-5} (°/$h^{1/2}$)

5. Conclusions

In this paper, we proposed a novel and significant dual-frame optomechanical gyroscope design, which integrates optical cavity interactions with mechanical resonant motion to achieve high angular resolution and sensitivity. We explained how our design overcomes the limitations and challenges of traditional MEMS gyroscopes that rely on electronic transduction and readout, such as noise, and stability issues. Such an optomechanical gyroscope comprises a pull-off electrostatic comb drive structure, test mass, and photonic crystal sensing structure. The operation principle of the new gyroscope including the Coriolis force transduction based on the optomechanical coupling is analyzed and discussed to prove that the angular vibration can be measured precisely. Moreover, the parameter selection and optimization of the sensitive structure and photonic crystal optomechanical cavity are studied utilizing finite element simulation. Under the appropriate electrostatic force, the optomechanical gyroscope can achieve *SF* = 22.8 mV/(°/s) and ARW = 7.1×10^{-5}(°/$h^{1/2}$) when *Pin* is 1 *mW*, and my is just 14ng. The gyroscope design proposed herein holds substantial promise for application in high-precision angular vibration measurements.

Future work will focus on experimental validation and potential applications in fields such as inertial navigation, geophysical exploration, and structural health monitoring where high angular precision is required.

Author Contributions: Writing—original draft preparation, software, conceptualization J.N.A.H.; review and editing, W.H.; review X.Y., S.Z., D.H; supervision, visualization, review and validation, G.W. and Y.H. All authors have read and agreed to the published version of the manuscript.

Funding: This work was supported in part by National Natural Science Foundation of China under Grants 61971113, and U2230206, in part by the National Key R&D Program under Grants 2018YFB1802102, and 2018AAA0103203, in part by the Guangdong Provincial Research and Development Plan in Key Areas under Grants 2019B010141001, and 2019B010142001, and in part by the Sichuan Provincial Science and Technology Planning Program of China under Grants 2021YFG0013, 2021YFH0133, 2022YFG0230, and 23ZDYF0110.

Institutional Review Board Statement: Not applicable.

Informed Consent Statement: Not applicable.

Data Availability Statement: Data underlying the results presented in this paper are available from the authors upon reasonable request

Conflicts of Interest: The authors declare no conflict of interest

References

1. T. Addabbo, A. Fort, R. Biondi, et al., "Measurement of angular vibrations in rotating shafts: effects of the measurement setup nonidealities," IEEE Transactions on Instrumentation and Measurement, vol. 62, pp. 532-543, March 2013.
2. M. Yang, Z. Liu, Y. Wang, C. Cai, and J. Yang, "Monocular vision-based multiparameter dynamic calibration method used for the low-frequency linear and angular vibration sensors," IEEE Transactions on Industrial Electronics, vol. 70, no. 5, pp. 5365-5374, May 2023.
3. A. Li, Z. Jing, Q. Liu, et al., "IFOG based on rhombic optical path difference bias configuration for high-frequency angular vibration measurement," IEEE Sensors Journal, vol. 22, no. 17, pp. 16892–16897, September 2022.
4. Y. Wang, R. Cao, C. Li, et al., "Concepts, roadmaps and challenges of ovenized mems gyroscopes: a review," IEEE Sensors Journal, vol. 21, pp. 92-119, 2021.
5. K. Larkin, M. Ghommem, M. Serrano, et al. "A review on vibrating beam-based micro/nano-gyroscopes," Microsystem Technologies, vol.27, pp. 1-25, 2021.
6. X. Ren, X. Zhou, S. Yu, et al., "Frequency-modulated MEMS gyroscopes: a review,". IEEE Sensors Journal, vol. 21, pp. 26426-26446, 2021.
7. Z. Li, S, Gao, L. Jin, et al., "Micromachined vibrating ring gyroscope architecture with high-linearity, low quadrature error and improved mode ordering," Sensors, vol.20, p. 432, 2020.
8. X.S. Liu, Z.C. Yang, X.Z. Chi, J. Cui, H.T. Ding, Z.Y. Guo, B. Lv, L.T. Lin, Q.C. Zhao, and G.Z. Yan, "A doubly decoupled lateral axis micromachined gyroscope," Sens. Actuator A Phys., vol. 154, pp. 218-223, 2009.
9. J. Xie, Q. Shen, Y. Hao, H. Chang, W. Yuan, "Design, fabrication and characterization of a low-noise Z-axis micromachined gyroscope," Microsyst. Technol., vol. 21 pp.625-630, 2015.
10. Trusov A A, Prikhodko I P, Zotov S A, "Low Dissipation Silicon Tuning Fork Gyroscopes for Rate and Whole Angle Measurements," IEEE Sensors Journal, vol.11, pp.2763-2770, 2011.
11. T. Zhang, B. Zhou, P. Yin, Z. Chen, R. Zhang, "Optimal Design of a Center Support Quadruple Mass Gyroscope (CSQMG)," Sensors, vol. 16, p. 613, 2016.
12. A. Sheikhaleh, K. Jafari, K. Abedi. "Design and Analysis of a Novel MOEMS Gyroscope Using an Electrostatic Comb-Drive Actuator and an Optical Sensing System," IEEE Sensor Journal, vol.19, pp. 144–150, 2019.
13. C. Trigona, B. Andò and S. Baglio, "Fabrication and Characterization of an MOEMS Gyroscope Based on Photonic Bandgap Materials," IEEE Trans Instrum Meas, vol. 65 pp. 2840-2852, 2016.
14. D. Xia, B. Zhang, H. Wu, Y. Wu, "Optimization and Fabrication of an MOEMS Gyroscope Based on a WGM Resonator Sensors," Sensors, vol. 20, p. 7264, 2020.
15. L. Yang, S. Zhao, J. Geng, B. Xue, and Y. Zhang, "Sensitivity enhancement of micro-optical gyro with photonic crystal," Chin. Phys. B, vol. 30 pp. 044208, 2021.
16. H. Zhang, M. Peng, X. Xu, H. Jing, "Anti-symmetric Kerr gyroscope," Chin. Phys. B, vol. 31, p. 014215, 2022.
17. T. Kippenberg, K. Vahala, "Cavity optomechanics: back-action at the mesoscale," Science, vol. 321, pp. 1172-1176, 2008.
18. M. Aspelmeyer, T. Kippenberg, F. Marquardt, "Cavity optomechanics," Rev. Mod. Phys, vol. 86, pp. 1172-1176, 2014.
19. LIGO Scientific Collaboration & Virgo Collaboration, "Observation of gravitational waves from a binary black hole merger," Phys. Rev. Lett. vol. 116, p. 061102, 2016.
20. Forstner, S., Knittel, J., Sheridan, E. et al. "Sensitivity and performance of cavity optomechanical field sensors," Photonic Sens, 2, 259–270, 2012.
21. E. Gavartin, P. Verlot, and T. J. Kippenberg, "A hybrid on-chip optome-chanical transducer for ultrasensitive force measurements," Nat. Nanotechnol. vol.7, pp. 509–514, 2012.
22. Y. Huang, J. G. Flor, Y. Li, W. Wang, D. Wang, N. Goldberg, J. Zheng, M. Yu, M. Lu, M. Kutzer, D. Rogers, D. Kwong, L. Churchill and C. W. Wong, "A chip-scale oscillation-mode optomechanical inertial sensor near the thermodynamical limits," Laser Photonics Rev. vol. 14, p. 1800329, 2020.
23. S. Davuluri, K. Li and Y. Li, "Gyroscope with two-dimensional optomechanical mirror," New J. Phys. vol.19, p. 113004, 2017.
24. K. Li, S. Davuluri, and Y, Li, "Improving optomechanical gyroscopes by coherent quantum noise cancellation processing," Sci. China Phys. Mech. Astron. vol. 61, p. 90311, 2018.

25. G. Li, X. Lu, X. Wang, J. Xin, and X. Li, "Optomechanical gyroscope simultaneously estimating the position of the rotation axis," J. Opt. Soc. Am. B, vol.39, pp. 98–106, 2022.
26. R. Madugani, Y. Yang, J. M. Ward, V. H. Le, and S. Nic Chormaic, "Optomechanical transduction and characterization of a silica microsphere pendulum via evanescent light," Appl. Phys. Lett. vol. 106, p. 241101, 2015.
27. H. A. Haus, "Waves and Fields in Optoelectronics. Englewood Cliffs," NJ, USA: Prentice-Hall, 1984.
28. A. Rasoloniaina, V. Huet, M. Thual, S. Balac, P. Féron, and Y. Dumeige, "Analysis of third-order nonlinearity effects in very high-Q WGM resonator cavity ringdown spectroscopy," J. Opt. Soc. Am. B, vol. 32, pp. 370–378, 2015.
29. C. Acar, A. Shkel, "MEMS vibratory gyroscopes structural approaches to improve robustness," New York: Springer Science+Business Media, 2009.
30. A. Krause, M. Winger, T. Blasius, Q. Lin and O. Painter, "A high-resolution microchip optomechanical accelerometer," Nat. Photonics, vol.6, pp. 768–772, 2012.
31. Oskooi A F, Roundy D, Ibanescu M, et al., "Meep: A flexible free-software package for electromagnetic simulations by the FDTD method," Computer Physics Communications, vol. 181, pp. 687-702, 2010.
32. Z. Djuri'c, "Mechanisms of noise sources in microelectromechanical systems," J. Microelectron. Reliab., vol. 40, pp. 919–932, 2020.
33. A. A. Trusov, I. P. Prikhodko, S. A. Zotov, and A. M. Shkel, "Low-dissipation silicon tuning fork gyroscopes for rate and whole angle measurements," IEEE Sens. J., vol. 11, no. 11, pp. 2763–2770, 2011, doi: 10.1109/JSEN.2011.2160338.
34. J. Xie, Q. Shen, Y. Hao, H. Chang, and W. Yuan, "Design, fabrication and characterization of a low-noise Z-axis micromachined gyroscope," Microsyst. Technol., vol. 21, no. 3, pp. 625–630, 2015, doi: 10.1007/s00542-014-2068-0.
35. T. Zhang, B. Zhou, P. Yin, Z. Chen, and R. Zhang, "Optimal design of a center support quadruple mass gyroscope (CSQMG)," Sensors (Switzerland), vol. 16, no. 5, 2016, doi: 10.3390/s16050613.
36. A. Sheikhaleh, K. Jafari, and K. Abedi, "Design and Analysis of a Novel MOEMS Gyroscope Using an Electrostatic Comb-Drive Actuator and an Optical Sensing System," IEEE Sens. J., vol. 19, no. 1, pp. 144–150, 2019, doi: 10.1109/JSEN.2018.2875076.